Experimental alteration of allanite at 200 °C: the role of pH and aqueous ligands

Axel Denys[1]*, Anne-Line Auzende[1], Emilie Janots[1]*, German Montes-Hernandez[1], Nathaniel Findling[1], Pierre Lanari[2], Valérie Magnin[1]

[1]Univ. Grenoble Alpes, Univ. Savoie Mont Blanc, CNRS, IRD, IFSTTAR, ISTerre, 38000 Grenoble, France

[2]Institute of Geological Sciences, University of Bern, Baltzerstrasse 1+3, CH-3012 Bern

*Corresponding authors:

Emilie Janots (emilie.janots@univ-grenoble-alpes.fr)

Abstract

Allanite is a major host of rare earth elements (REE) in the continental crust. In this study, reaction mechanisms behind allanite alteration are investigated through batch experiment runs on natural allanite grains in carbonate-bearing hydrothermal fluids at 200 °C, with initial acidic (pH=4) or alkaline (pH=8) conditions and with different aqueous ligands (120 mM of F, Cl, P or S). Time-series experiment runs in F-doped systems at different durations between 15 and 180 days reached a steady state at 120 days. The pH efficiently controls the allanite alteration process, with initial high pH, alkaline conditions being more reactive (75% alteration compared to 25% under acidic conditions). The ligand also significantly influences the alteration process under initial acidic conditions with P-doped system (70%) almost non-reactive for the Cl- and S-doped systems (< 5%). In the alteration rim, REE are mainly redistributed in REE-bearing phases either as carbonates (F-doped) or phosphates (P-doped). The relatively flat REE-normalized patterns of the recovered experimental fluids suggest a fractionation of LREE over HREE during the course of the alteration reactions. It is proposed that secondary REE-mineral precipitation at the reaction front creates a local disequilibrium in the solution and a steep chemical gradient promoting allanite dissolution and thus its alterability.

Keywords: allanite; hydrothermal alteration; rare earth elements (REE); batch experiment; mineral replacement; REE-fluorocarbonate; monazite

1 Introduction

Allanite, a mineral of the epidote group with the ideal formula $CaREEFe^{2+}(Al, Fe^{3+})_2(Si_2O_7)(SiO_4)O(OH)$, is a major REE-carrier mineral in the continental crust, with preferential incorporation of the light REE (LREE: La to Gd) over the heavy REE (HREE: Tb to Lu + Y). Primary allanite occurs as an accessory phase in magmatic and metamorphic rocks (Gieré and Sorensen, 2004 and references therein). It is a good petrological proxy and geochronometer for metamorphic processes (e.g. Engi et al., 2017), magma sourcing (e.g. Anenburg et al., 2015), or mineralisation under hydrothermal conditions (e.g. Pal et al., 2011). Allanite has also been described as the main primary REE and U source in supergene and hydrothermal systems (Caruso and Simmons, 1985; Berger et al., 2008; Ichimura et al., 2020), reaching economic levels (Chabiron and Cuney, 2001; Corriveau et al., 2007). Hydrothermal alteration of allanite is common (Poitrasson et al., 2002) and often occurs as partial replacement of primary allanite by secondary REE-minerals. These include fluorocarbonates (e.g. Middleton et al., 2013), phosphates (Berger et al., 2008), and silicates (Smith et al., 2002). Frequently, secondary Th-minerals are also described in association with allanite replacement (Buda and Nagy, 1995; Middleton et al., 2013). As a main REE-host, these alteration reactions are thus important for understanding REE mass transfer, with their economic implications as strategic metals. Furthermore, understanding associated actinide mobility in REE-rich hydrothermal systems is also crucial, because it can be decisive for REE-mining (as by-products or nuclear waste).

It is widely accepted that the greater sensitivity of allanite to alteration, compared to that of epidote (Price et al., 2005), is partly due to its metamict state, which is caused by α-particle bombardment damaging the structure, even for a low Th and U content (Ewing et al., 1987; Ercit,

2002). The role of other inherent factors, such as the crystal chemistry of the allanite and the physicochemical properties of the fluid, remains poorly understood. While numerous examples of natural allanite alteration have been reported, its experimental reactivity in the presence of hydrothermal fluids has received little attention, only at high pressure and high temperature conditions (Krenn et al., 2012) or as a product of monazite and xenotime alteration (Budzyń et al., 2011; 2017). In order to fulfil this gap, allanite alteration experiments have been conducted on natural homogeneous crystalline grains in the presence of carbonate-bearing hydrothermal fluids doped with various ligands (120 mM of F, Cl, P, S) under initial acidic and high pH alkaline conditions at 200 °C and P_{sat} for durations from 15 to 180 days. The role of added ligands was investigated for initial acidic conditions, (pH around 4 at room temperature), common under hydrothermal conditions (Seward et al., 2014). The investigated ligands are elements of importance for REE mobility in hydrothermal systems due to strong aqueous complexation at 200 °C (Gammons et al., 1996; Migdisov and Williams-Jones, 2002, 2008; Migdisov et al., 2009). The kinetics of the alteration reactions were investigated through time-dependent experiments using both acidic and high pH alkaline fluids, (pH = 8 at room temperature), in the presence of F. In this study, the experimental alteration of allanite is strongly controlled by the fluid composition and the precipitation of secondary REE-minerals in the form of fluorocarbonates and phosphates.

2 Analytical methods and experimental procedure

2.1 Starting material

All experiments were performed using fragments from a monocrystal of allanite ~~(20 mm-~~ Ce (henceforth allanite) from the Frontenac formation in the Central Metasedimentary Belt of the Greenville Orogen (Ontario, Canada). Crystallisation ages, based on associated titanite U-Pb geochronology, ~~range from~~are around 1157 - 1178 ~~to 1157~~ Ma (Mezger et al., 1993). The composition, determined by EPMA, is homogeneous, and corresponds to an intermediate composition between ferriallanite and allanite, with a general formula: $Ca_{1-1.2}REE_{0.6-0.8}Al_{1.5-1.7}Fe^{3+}_{0.1-0.5}Fe^{2+}_{0.8-1.1}Mg_{0.1}Si_{3.1-3.3}O_{12}(OH)$ (Table S1, supp. mat.). Radionuclides contents ~~are~~range such as 0.~~53~~36-0.79 wt.% ThO_2 and ~~0.06 wt.%~~ UO_2 mostly below detection limit.

The crystal was crushed manually and then grinded mechanically using a planetary micro-mill Fritsch Pulverisette 7. To ensure maximized kinetics and yet a suitable grain size for post-experimental characterization, we selected an initial grain size of 20-50 µm after sieving. Traces of REE-carbonates in micro-cracks (observed by SEM but not detected on X-ray diffraction pattern) were removed by soaking the allanite powder in a 1M acetic acid solution in an ultrasonic bath for 10 min. After centrifugation (3500 rpm, 10 min), the solid residue was filtered through a 2.7 µm glass fibre filter and dried overnight at 50°C. The material was stored in spectroscopic plastic tubes in the dark at ambient temperature.

2.2 Experimental procedure

Experiments were conducted by reacting 150 mg of powdered allanite (Fig. S4, supp. mat.) with 1.5 mL of the aqueous solution (fluid/solid ratio = 10) in 3 mL Teflon cell reactors sealed into a steel autoclaves without agitation ("static batch reactor") and placed in a multi-oven at 200 °C ($P_{sat} \approx$ 16 bar or 16 bar + pCO_2, when CO_2 was added). However, pCO_2 varies during alteration and these variations were not quantified. Acidic solutions with an initial pH = 4 were obtained by adding to ultrapure water 99.9% certified pure carbonic ice (around 30 mg). For alkaline systems, ultrapure water was replaced by 1.5 mL of a 1 M $NaHCO_3$ solution (pH = 8.7, Lafay et al., 2014). These solutions were mixed with 120 mM~~,~~ (equivalent of the REE molar content in allanite~~),~~) of F~~,~~ (introduced as solid NaF), P (as Na_3PO_4~~,~~ $12H_2O$), S (as Na_2SO_4) or Cl (as NaCl). A first time series of experiments using NaF as ligand in acidic and alkaline systems was performed (15, 30, 60, 120, and 180 days) to investigate the kinetics of the reaction processes (**Table 1**). Experiments with other ligands were run for 120 days. At the end of each experiment, the sealed reactor was rapidly quenched in cold water. Recovered solutions were carefully collected with a syringe, filtered to remove solid residue (0.2 µm), diluted 5 times in ultra-pure water slightly acidified with nitric acid and immediately stored at 4 °C in a ion-free~~-ion~~ tube for further characterization. Residual solid was collected, dried at 60 °C for one night, weighted and stored at ambient temperature. A fraction of each solid run product was mounted in epoxy resin and finely polished (mirror surface) for microscopic and electron microprobe analyses.

2.3 Solid characterization methods

2.3.1 X-Ray Diffraction (XRD) and Rietveld refinement

Mineral modal abundances of initial and post-experimental solids were characterized by XRD at ISTerre (Grenoble, France). Samples were grounded in ethanol using a McCrone micronizing mill, oven-dried overnight and prepared as a randomly oriented mount. The XRD patterns were recorded with a Bruker D8 powder diffractometer equipped with a SolXE Si(Li) solid state detector from Baltic Scientific Instruments using CuKα_1+2 radiation. Intensities were recorded at 0.026° 2θ step intervals from 5 to 90° (10 s counting time per step). Eva Bruker software associated with the ICCD pdf database was used to determine the modal composition of the powder on a significant part of the recovered solid product for all alteration experiments. This enables to distinguish between the different REE-minerals in the solid product. Rietveld refinement with Profex/BGMN software was then performed to precisely quantify mineral abundances. The quality of the Rietveld refinement is assessed by the χ^2 factor, which lies between 2.5 and 4 for all experiments.

2.3.2 Scanning Electron Microscopy (SEM)

The mineral distribution and microstructure of the experimental solids were investigated by using a ZEISS Gemini 500 SEM. The measurements were carried out in high-vacuum mode using a high tension (EHT) of 3 kV for a working distance (WD) between 3.4 and 4.8 mm. Samples were sputtered with a 15 nm thick cover of Au-Pd. Complementary investigations were performed using the conventional environmental SEM Tescan Vega 3. The measurements were

carried out in high-vacuum mode (9.9 ~~x~~× 10^{-9} bar), using an accelerating voltage of 16 kV, with 90 nm spot size and 15 mm working distance. Samples were sputtered with 20 nm of carbon. The microscope is equipped with a 30 mm^2 Energy Dispersive X-Ray Spectroscopy (EDS) manufactured by Rayspec with SamX's electronic system and software.

2.3.3 Electron probe micro-analyser (EPMA)

Quantitative chemical analyses of initial and post-experimental allanite and secondary products (when the grain size was suitable) were carried out using a JEOL JXA-8230 electron probe micro-analyser (EPMA) equipped with five wavelength-dispersive spectrometers (WDS) at ISTerre (Grenoble, France). Analytical conditions were 15 kV acceleration voltage, 12nA beam current, and 1 to 5 µm beam size (details in Table S3, supp. mat.). The ZAF correction procedure was applied using the JEOL software for quantitative analysis. The detection limits range between 0.01 and 0.04 wt% using the 2σ criterion (Batanova et al., 2018).

2.3.4 Trace element analysis (LA-ICP-MS)

Trace element analysis of allanite was performed at the Institute of Geological Sciences (University of Bern) using a laser ablation inductively-coupled plasma mass spectrometry (LA-ICP-MS), which consisted of a Geolas Pro 193 nm ArF excimer laser coupled to an Elan DRC-e quadrupole ICP-MS. A He-H_2 gas mixture (1 and 0.008 L/min respectively) was used as the aerosol transport gas. Allanite trace element analyses were performed with laser beam diameters of 16, 24, and 32 µm, frequencies of 9 and 7 Hz, and energy densities on the sample of 5.0 J/cm^2.

Sample analyses were calibrated using GSD-1Gg and accuracy was monitored using a reference glass NIST glass SRM 612 (Jochum et al., 2005, 2011). Data reduction was performed using the SILLS software package (Guillong et al., 2008) and LOD values obtained with the method of Pettke et al. (2011).

2.4 Fluid characterization methods

2.4.1 Inductively-coupled Plasma Spectrometry

All recovered solutions were stored using metal-free tubes (VWR). For an accurate quantification of trace elements, measurements were performed by ICP-MS using a Thermo Scientific XSERIES 2 spectrometer. Recovered solutions were diluted 3 times with 2% HNO_3 solution to a volume of 6 mL. Finally, 0.5 mL of an In solution was systematically added as an internal standard to correct for the drift of the ICP-MS. Collision Cell Technology (CCT) was used for some elements (Ca, Fe, and Mn) in order to reduce polyatomic interferences with 5% H_2 in He gas. Measurements quality was evaluated by duplicating the measurement of standards that were analysed five times on the ICP-MS. Calculations, to extract concentrations from the integration of peak signals, were performed off-line. Reproducibility depends on the nature of the analysed element. It ranges between 1 and 19% for the REE and from 3 to 30% for other trace elements. The detection's limits (D.L.) are defined as 3 times the blanks average. All data below the detection limit were excluded. Because the torch for ICP-MS was sheathed in quartz, Si was then determined by atomic emission spectrometry (ICP-AES) using a Perkin Elmer Optima 3000 DV ICP-AES. Solutions were diluted five times using a 2% HNO_3 solution providing the

minimum analysable volume. The same HNO_3 solution was used to prepare standards and blanks. The analytical error for Si is 8 %.

2.4.2 Capillary electrophoresis (CE)

The anionic content (Cl^-, SO_4^{2-}, F^-, PO_4^{3-}, HCO_3^-) in the recovered solutions was quantified using a capillary electrophoresis (CE) system by WATERS®. The CE apparatus was equipped with a fuse capillary (75 µm i.d. ~~x~~× 60 cm total length) and a diode detector. The CE was operated at 20 °C and at a voltage of 20 kV. Electrophoregrams were recorded with the indirect mode detection at 254 nm using an Hg lamp. The background electrolyte (BGE) was composed of 4.6 mmol/LNa_2CrO_4 solution, 0.5 mmol/L OFMOH™ from WATERS™, and an H_3BO_4 solution (pH = 8.0). Prior to each measurement series, the capillary was conditioned by flushing with 1 mol/L NaOH and 0.1 mol/L NaOH (5 min each) followed by a 10 min flush with deionized water and a BGE solution (15 min flush). The capillary was preconditioned prior to each measurement by flushing the BGE for 1 min. All samples were measured in duplicate using hydrostatic injection mode.

3 Results

3.1 Allanite alteration as a function of the initial pH

The role of initial pH was investigated by time-series experiments in order to evaluate, together with the final alteration extent, the kinetics of the reaction. The experiments were performed for F-doped system at a duration of between 15 and 180 days under initial acidic and high pH alkaline conditions (Table 1).

The recovered experimental solids, characterized by X-ray diffraction, displayed alteration evidence with secondary phases in the run products (Fig 1). The extent of alteration was estimated on the basis of remaining allanite in the recovered samples. The constancy of the allanite composition between the final and initial materials (Table S1 - Supp. Mat) attested to no secondary allanite/epidote precipitation. The reaction progress was estimated from the allanite abundance. The run products modal composition showed that the kinetics and extent of alteration greatly varied with the initial pH (Fig. 1). The alteration rate was much higher in the high pH alkaline system, with 65% alteration reached within the first 15 days and a rapid stabilisation at around 70 to 75% alteration from 30 to 120 days. In contrast, the extent of alteration in the acidic experiments was scarce after 15 days and only achieved 25% alteration for the longest durations (120 and 180 days). However, under both the acidic and high pH alkaline conditions, with a F-doped solution, the same mineral phases grew at the expense of allanite (Fig. 1): analcime (Na-Al silicate), hematite (Fe_2O_3), and REE-bearing carbonates (Table 2). The REE-bearing carbonates, determined from XRD analyses, changed depending on the initial pH of the solution. They consisted of (1) bastnäsite (general formula: $LREECO_3F$) and synchysite (general formula:

211 $CaLREE(CO_3)_2F$) under acidic conditions and (2) a burbankite-group mineral (thereafter referred
212 as BGM, with the general formula: $(Na,Ca)_3(Sr,Ba,Ce)_3(CO_3)_5$) and REE-fluorocarbonates with
213 parisite (general formula: $CaLREE_2(CO_3)_2F_2$) associated with bastnäsite and minor synchysite in
214 the high pH alkaline system. Besides these phases, fluorite (CaF_2) appeared in the acidic
215 experiments, while calcite ($CaCO_3$), smectite, and minor nordstrandite (general formula:
216 $Al(OH)_3$) crystallized in the high pH alkaline system. High REE contents up to 2 wt% and 8 wt%
217 $(REE+Y)_2O_3$were measured in fluorite and calcite, respectively (Table 2; Table S2 supp. mat.).

218 The microstructures of the recovered solids differed depending on the initial pH, which
219 can be attributed to the reaction progress. In acidic system, due to low alteration rate (15 days),
220 the initial shape of the allanite grains, characterized by typical conchoidal edges, was mostly
221 preserved while fluorite and analcime crystals grew around allanite from the bulk fluid (Fig. 2a).
222 The allanite surface was pitted~~, however,~~ and covered by smectite ~~in a typical honeycomb~~
223 ~~structure~~ (Fig. 4b). At this stage, REE-(fluoro)carbonates were restricted to inherited fractures in
224 the allanite. A higher reaction extent (25%) in the acidic system (120 days), resulted in alteration
225 rims surrounding some of the allanite grains. Their surfaces were characterized by a pervasive
226 saw-tooth shaped reaction front, highlighting more extensive dissolution (Fig. 2b). Reaction rims
227 were sequentially composed of discontinuous layers of hematite followed by nanocrystals with
228 the granular and acicular shape of REE-fluorocarbonates penetrating through the dissolving
229 allanite at the reaction front and filling newly-opened fractures (Fig. 2c).

230 In the high pH alkaline run products, the allanite grain shape is preserved on the micro-
231 scale, surrounded by layers of complex micro-textures. The morphologies and textures described
232 for the run product from the 15-days experiment do not significantly change compared to the

longer duration experiments. Allanite has penetrative reaction rims that can reach up to 10 µm thick (Fig. 2d). They were delimited by complex microstructures at the reaction front, such as nanoscale etch pits or saw-tooth surfaces (Fig. 2e). Close to the reaction front, REE-fluorocarbonates also precipitated at the surface, within the etch pits or in inherited microfractures, with nano-granular, acicular, or prismatic shapes (Fig. 2e). The sub micron size of these phases prevented quantitative chemical analyses by EMPA. The allanite surface was overlain with a thin layer of hematite crystals of around 10 to 500 nm in size. Smectites were also ubiquitous and clearly identifiable by their fibrous (honeycomb) morphology and platelet growth oriented towards the fluid. The burbankite-group minerals (BGM) occur as microscale euhedral crystals that randomly precipitated from the reactive bulk fluid (decoupled from the allanite replacement products). They are mainly prismatic and more or less elongated with a size generally varying from ca. 5 to 30 µm in size (Fig. 2f). The BGM crystals commonly display a zonation with respect to the REE content which is anti-correlated with respect to Ca (Fig. S5, supp. mat.). They have a higher LREE than the initial allanite, but with Sm and Y below the detection limit (Table 2). Calcite precipitates as aggregates of euhedral crystals 10 to 20 microns in size or intergrown with relic allanite (Fig. 2f).

3.2 Allanite alteration as a function of ligands

To investigate the effects of ligands on the alteration of allanite, experiments were run under the initial acidic conditions with P-doped, S-doped and Cl-doped solutions for 120 days (Table 1). Similar to that observed for the pH, the reaction progress was also significantly affected by the ligands (Fig. 3). The most reactive system was the P-doped one, which achieved 73% allanite alteration. This reaction extent was similar to that seen in the F-doped system under high pH

alkaline conditions (75%),% of reaction), but much higher than that obtained under similar acidic conditions (23%,)% of reaction) over the same duration (120 days). The S- and Cl-bearing systems were notless reactive compared to the others with less than 5% secondary minerals.

In the reactive P-doped experiments, analcime and hematite were present in major proportions in the recovered solid, as for the F-doped system. Smectite was also an alteration product of allanite, as in the high pH alkaline system. The main difference between the P- and F-doped systems was the nature of the mineral phases that accommodated REE and Ca, such as monazite (general formula $LREEPO_4$, 21% of solid product) and hydroxyapatite (general formula $Ca_5(PO_4)_3OH$, 18% of solid product). The alteration microstructures were very similar to those previously described in the F-bearing system. Allanite was largely affected by dissolution, as illustrated by the numerous etch pits scattered on the allanite surface (Fig. 4a). Allanite alteration resulted in thick reaction rims made up of a nano-mixture of monazite-hematite and hydroxylapatite with an apparent microscale spatial distribution from the reaction front towards the reactive fluid (Fig 4b). Sub-micron monazite crystals precipitated directly at the interface with the allanite (Fig. 4c). Similar to the F-doped systems, hematite occurred as a thin, quasi-continuous corona around the allanite grains. Finally, euhedral micrometric-sized grains of hydroxylapatite, mixed with smectite filaments, which probably formed during the quench, are seen along the outer edge of the alteration rim (Fig. 4b and c). Analcime remains the major alteration phase, and takes the form of large grains embedding relict allanite along the allanite reaction rims (Fig. 4a).

3.3 Recovered fluid chemistry

Beside solid product characterization, the fluid composition was also analysed for each experiment (Table 3; Fig. 5). While the fluid compositions can be modified by internal and external factors through the course of the reaction (water consumption by alteration products, permeability limits of the Teflon reactors, quenching effects), the reproducibility of the results supports the general qualitative significance of the fluid chemistry dataset.

In time-series experiments, the final fluid compositions indicated that the experiments under high pH alkaline conditions were already in a steady-state (approaching constant concentrations of all measured elements with time) after 15 days (Fig. 5b), which is in agreement with the mineralogical results. In the initially ~~acid~~acidic system, elemental concentrations of Ca, REE, Th~~,~~ and U evolved until reaching a near plateau only after 120 days (Fig. 5a). At that stage, Si, Al, and Ca reached similar concentrations in the F-doped acidic and high pH alkaline systems, whereas REE, U~~,~~ and Th were lower in the acidic system compared to the high pH alkaline system by 2 to 4 orders of magnitude.

In the P-doped system, which was the most reactive system under acidic conditions, elemental concentrations are similar to the concentrations of the F-doped in the acidic system at 120 days (Fig. 5c). In the unreactive Cl- and S-doped systems, Si and REE concentrations are comparable with those measured in the F- and P-doped systems under acidic conditions. The other elements were generally at lower concentrations.

In terms of REE, the chondrite-normalized patterns plot relatively flat for the high pH alkaline systems (Fig. 6). ~~There is~~In acidic fluids, patterns plot also relatively flat but with a

~~MREE~~slight depletion ~~compared to LREE~~in Sm, Gd and ~~HREE in acidic fluids~~Dy, with no dependence on the ligand.

4. Discussion

4.1 Allanite alteration mechanisms

In the batch experiment runs (Table 1), the alteration of allanite ranges from a very limited (< 5%) up to a very extensive (77%) degree depending on the fluid chemistry after 120 days. The pH has the first effect on the alteration of allanite, as the kinetics for the high pH alkaline system are fastest (65%) after 15 days, and the more advanced (70–75%) after 120 days in the two time-series experiment runs conducted in an F-doped system. Under acidic conditions, the nature of the ligand significantly affects the extent of alteration. The presence of P enhances the allanite alterability, reaching 73% of the reaction rate after 120 days, while allanite reactivity is minor in the Cl- or S-doped systems (< 5%). F-doped systems display moderate alteration at the same duration (25%). Higher allanite reactivity in a high pH alkaline fluid shows that high pH fluids efficiently promote silicate dissolution rates, while dissolution is more limited in near neutral fluids (Hellmann, 1994). This effect is also demonstrated for epidote group minerals (Rose, 1991). Phosphorus seems to have a similar effect on allanite, though with a lower extent of alteration.

In the most reactive systems (high pH alkaline and P-doped conditions), the alteration of allanite is promoted by increasing dissolution coupled with the precipitation of other minerals. On one hand, dissolution can be promoted due to a solubility change for the dissolving elements in the bulk solution, by modifying element complexation, the concentration in the solution, and the

317 chemical affinity per the dissolution reaction between allanite and the fluid. On the other hand,
318 the mineral microstructures evidenced here also point to the crucial role of secondary precipitation
319 on the alteration rate. Alteration microstructures from highly altered ~~run~~experiment products show
320 well-developed dissolution features (etch pits, fractures, porosity) with a penetrative replacement
321 by an alteration rim made up of secondary minerals with a complex mineralogical zonation.
322 General preservation of the initial pristine shape of allanite suggests a mechanism of replacement
323 by interfacially coupled dissolution-precipitation (Putnis, 2002; Putnis and Putnis, 2007;
324 Hellmann et al., 2012), which indicate disequilibrium between the solid and the fluid (Putnis,
325 2009; Ruiz-Agudo et al., 2014). Such alteration processes can lead to an apparent incongruent
326 dissolution due to a preferential precipitation of low solubility phases (with different composition
327 than the altered phase) at the alteration interface (Ruiz-Agudo et al., 2012). Such apparent
328 incongruent dissolution has already been demonstrated for epidote dissolution (Kalinowski et al.,
329 1998), and seems also to apply here to allanite alteration as seen by the mineralogical gradation
330 from the reaction front to the bulk solution. In the reaction rim, the precipitation of submicron,
331 low-solubility secondary phases takes in elements from the solution and changes their
332 concentration at the reaction interface. This is the case for hematite, which nucleates as a thin rim
333 at the interface with the allanite. But this is particularly true for REE-mineral phases, (REE-
334 fluorocarbonates or monazite depending on the ligand), which also occur as a discontinuous rim
335 of nano-scale crystallites propagating anisotropically inward into the pristine grain and along
336 fractures in the allanite. The growth of other main phases with a higher solubility in the solution,
337 e.g. analcime, fluorite, and calcite, is spatially decoupled from the alteration interface with
338 precipitation from the bulk solution as larger euhedral crystals. Such precipitation from the bulk
339 fluid away from the rim of the dissolving mineral have been described in other alkaline systems

(Lafay et al., 2014, 2018). In the batch experiment runs, the preferential precipitation of REE-phases at the reaction front is proposed to efficiently maintain significant dissolution rates by producing steep concentrations gradients in the fluids close to the reactive surface, which act to renew the solutions (Ruiz-Agudo et al., 2016; Frugier et al., 2008).

Coupled with the chemical gradient at the interface, the precipitation of REE-mineral phases will further strongly modify the geometry of the reaction front. The complex microstructures at the reaction interface, with etch pits, indentations, and secondary fractures, are the result of reaction-induced fracturing due to molar volume change and the force of crystallization during the replacement of allanite by secondary phases (e.g. Jamtveit et al., 2009; Lafay et al., 2018). This increase of the reactive surface also enhances allanite dissolution.

In the two non-reactive systems (Cl- and S-doped), there was very limited precipitation of secondary phases (< 5%). In batch experiment runs, this drop in the dissolution rates can occur when element concentrations progressively approach saturation in the fluid or when precipitation of an inert passivation layer isolates the reacting mineral from the reactive fluid (Montes-Hernandez et al., 2012). In unreactive systems, secondary precipitation observed at the grain surface is sufficiently low such that allanite remains accessible to the fluid throughout the experiment runs. In contrast, concentrations in fluids similar to those of reactive systems indicate that they reach conditions approaching saturation. Since precipitation of analcime and hematite is not chemically restricted, the only limiting factor here appears to concern the stability of the REE-phases.

In the investigated reactive systems, the ~~precipitated~~precipitation of secondary REE-phases is thus proposed to be the main driving force behind allanite alteration by lowering the

activities of REE in the interfacial fluid. In the absence of efficient REE-mineral precipitation (Cl- and S-doped) at the allanite interface, "steady state" concentrations measured in the bulk fluid are assumed to be more readily reached, thus decreasing reaction rates. Therefore, allanite alteration remains low. These results are in good agreement with natural observations. The secondary, experimental REE-mineral phases, i.e., REE-fluorocarbonates and/or REE-phosphates ~~associated with~~are typical of low-temperature alteration products (e.g. Berger et al., 2008; Ondrejka et al., 2018).

4.2 REE, Th, and U mobility and fractionation during allanite alteration

In all reactive systems, comparison between a simple mass balance calculation from the low REE concentrations in the recovered fluid and the allanite composition and alteration rates ~~indicate~~indicates that the REE released during alteration are mostly in secondary phases. Seventy percent allanite alteration would provide 100 µmol of the REE released in high pH alkaline experiment runs. However, the REE contents in the final fluids are 4 orders of magnitude below. The main REE-minerals (REE-carbonates or REE-phosphates identified by XRD), occur as submicronic crystals in the alteration rim, preventing accurate determination of their REE contents. Based on the theoretical compositions of REE-fluorocarbonates and monazite, along with their XRD modal abundance, rough mass balance calculations confirm that they are a major sink for the REE released by allanite. In the P-doped system, the hydroxylapatite grains are also too small for determining their REE content though it could be up to a few wt.% (Budzyń et al., 2017).

While the composition of secondary phases in the altered rim cannot be analysed precisely for their REE ~~compositions~~contents, minerals precipitating from the bulk-fluid are large enough for evaluating their REE content by EPMA. In F-doped systems, fluorite represents 25% of the secondary products, and can incorporate up to 1-2 wt.% ~~REE~~REE_2O_3. The REE content in fluorite has been extensively studied in hydrothermal systems (Möller et al., 1998; Schwinn and Markl, 2005; Schönenberger et al., 2008; Gob et al., 2011), in economical REE-deposits, such as the Bayan Obo complex (Xu et al., 2012), or by thermodynamic modelling (Kolonin and Shironosova, 2007). It shows that REE in fluorite, while extremely variable, but can reach up to > 10 wt.% in yttrofluorite (Pekov et al., 2009). Although a coupled substitution involving Na is often considered preponderant for incorporating the REE ~~within~~in fluorite, i.e. $REE^{3+} + Na^{+} \leftrightarrow 2\ Ca^{2+}$ (Möller et al., 1998), there is no real correlation between the REE and Na contents in the fluorite from these experiments, despite the high Na concentrations. The BGM (identified from XRD) precipitating from the bulk-fluid also accommodate significant REE, but with Na concentrations that are ~~too low~~significantly lower compared to burbankite *sensu stricto* (Beloviskaya and Pekov, 2004). The BGM are zoned with a typical hourglass sector zoning suggesting crystallographic control on REE incorporation (Fig. 2f). Integration of the REE is directly correlated to the size and geometry of the crystallographic sites, which favour the LREE in calcic minerals, such as tourmaline (van Hinsberg et al., 2010). Burbankite is a hydrothermal mineral encountered in alkaline pegmatites and associated carbonatites (Zaitsev et al., 2002). In the experiments, the precipitation of BGM minerals is probably favoured by the Na concentration in the fluid. Finally, the REE concentrations in the calcite are considerably higher than those normally encountered in nature (Stipp et al., 2006) but are thermodynamically stable (Rimstidt et al., 1998) as has been experimentally demonstrated (Toyama and Terakado, 2014; Gabitov et al., 2017). In calcite, two

coupled substitution mechanisms are proposed as follow (Perry and Gysi, 2018), i.e. $REE^{3+} + Na^{+} \leftrightarrow 2Ca^{2+}$ and $2REE^{3+} + \square \leftrightarrow 3Ca^{2+}$. The composition of the calcite produced in these experiments ~~indicate~~indicates that both mechanisms occur under the experimental conditions of this study (Fig. S5, supp. mat.).

4.3 REE fractionation between fluid and solid

Though the REE are mainly stored in secondary phases, minor REE concentrations have been recovered in the fluids. Though precise quantitative fluid concentrations are limited by the batch experimental setup, our qualitative results clearly indicate a significant difference in REE fractionation between the solid and the fluid whatever the pH and the complexing ligands. Experimental fluids display relatively flat chondrite normalized REE spectra, indicating that the experimental alteration of allanite ultimately produces a fluid enriched in HREE relative to the initial LREE-rich allanite composition. This implies in turn the preferential fractionation of LREE over HREE in the secondary mineral precipitates relative to the fluid. This is in good agreement with the limited incorporation of HREE in fluorocarbonates and monazite, as demonstrated for T < 450 °C (Heinrich et al., 1997; Poitrasson et al., 2000; Janots et al., 2008; Budzyń et al., 2010; 2017; Grand'Homme et al., 2018). Also, secondary minerals that precipitate from the bulk-fluid (calcite, fluorite, BGM) are enriched in LREE over HREE but with lower La/Y compared to allanite, again supporting the fractionation of the LREE over the HREE in the bulk fluid compared to fluid at the reaction front. In these secondary mineral phases, the Y values are typically at the

same level as in allanite, which suggests that the HREE are more mobile compared to the LREE, as seen in numerous natural environments, e.g. during monazite alteration (Hentschel et al., 2020).

The fluid compositions measured in this study have numerous implications for REE deposits. Here the flat or gently incurved REE normalized pattern indicates that REE are not released congruently but that speciation in the fluids or precipitation of secondary products favour HREE fractionation over LREE in the fluid compared to the initial allanite composition.

4.4 Th and U behaviour during allanite alteration

Actinides seem to mostly partition into the fluid as opposed to secondary minerals. Simplified qualitative calculations show that virtually all the U released by allanite goes into the fluid under these conditions. Actinide concentrations are higher in the high pH alkaline system (with higher carbonate activities) than in the acidic system. This agrees rather well with studies that show that the solubility of actinides increases with the concentration of the aqueous carbonate or phosphate ligands (Rai et al., 1994; Sandino and Bruno, 1998). Recent studies also show that actinides can be highly mobile in the presence of ligands such as S-, Cl-, or F-complexes for temperatures close to 200 °C (Nisbet et al., 2018, 2019; Migdisov et al., 2019). In the experimental runs under initial acidic conditions, U release is however at least 1 to 2 orders of magnitude lower than that under high pH alkaline conditions. Regardless of the chemical system, Th is systematically lower in the fluid compared to U while it is higher in the starting allanite, indicating U/Th fractionation during allanite alteration. According to Rai et al. (1994), ThO_2 solubility is higher than that of UO_2, suggesting that tetravalent U is likely oxidized in its hexavalent state during the allanite alteration reaction. Preferential incorporation of tetravalent Th in secondary

REE-mineral phases may in turn enhance Th/U fractionation between the fluid and secondary products as observed in natural monazite and allanite precipitated from hydrothermal systems (Janots et al., 2012).

5. Conclusions

Allanite has a complex composition and its experimental alteration under low temperature conditions results in a high diversity of mineralogical assemblages and microstructures. Allanite can be highly reactive in certain fluids, reaching more than 75% of alteration at 200 °C and $P_{sat} \approx$ 16 bar, after only 15 days. The pH and the nature of the complexing ligand added to the fluid will strongly affect the alteration rate of the allanite, with the high pH alkaline system being the most reactive. In carbonate-bearing fluids, F and P will promote allanite alteration, while allanite shows negligible alteration in the presence of Cl and S. The main driving force behind the alteration of allanite resides in the precipitation at a reactive front of secondary REE-minerals, whose chemistry depends on the complexing ligands. These precipitated minerals maintain a local disequilibrium close to the reaction interface between the fluid and the solid, thus sustaining allanite dissolution. Though REE are mostly stored in the secondary mineral phases, there is a preferential fractionation of the LREE over the HREE into the solid compared to the fluid while U is strongly partitioned into the fluid.

Acknowledgments

Electron microscopy was performed with the kind help of Rachel Martin at the CMTC characterization platform of Grenoble INP supported by the Centre of Excellence of Multifunctional Architectured Materials "CEMAM" n°AN-10-LABX-44-01 funded by the "Investments for the Future" Program. We are very grateful to S. Campillo, S. Bureau and M. Lanson for fluid analyses and following discussions. This paper benefited from insightful comments of C. Cordier, F. Brunet and A. Fernandez-Martinez. This PhD work was further supported by the TelluS Program of CNRS/INSU and local BQR funding. The work was mainly done in ISTerre (Université Grenoble Alpes), which is part of Labex OSUG@2020 (ANR10 LABX56).

References

Anenburg, M., Katzir, Y., Rhede, D., Jöns, N., Bach, W., 2015. Rare earth element evolution and migration in plagiogranites: a record preserved in epidote and allanite of the Troodos ophiolite. Contributions to Mineralogy and Petrology 169.

Batanova, V.G., Sobolev, A.V., Magnin, V., 2018. Trace element analysis by EPMA in geosciences: detection limit, precision and accuracy. IOP Conference Series: Materials Science and Engineering. 304, 012001.

Belovitskaya, Y.V., Pekov, I.V., 2004. Genetic mineralogy of the Burbankite group. New Data on Minerals 39, 15.

Berger, A., Gnos, E., Janots, E., Fernandez, A., Giese, J., 2008. Formation and composition of rhabdophane, bastnäsite and hydrated thorium minerals during alteration: Implications for geochronology and low-temperature processes. Chemical Geology 254, 238–248.

Budzyń, B., Harlov, D.E., Kozub-Budzyń, G.A., Majka, J., 2017. Experimental constraints on the relative stabilities of the two systems monazite-(Ce) – allanite-(Ce) – fluorapatite and xenotime-(Y) – (Y,HREE)-rich epidote – (Y,HREE)-rich fluorapatite, in high Ca and Na-Ca environments under P-T conditions of 200–1000 MPa and 450–750 °C. Mineralogy and Petrology 111, 183–217.

Budzyń, B., Harlov, D.E., Williams, M.L., Jercinovic, M.J., 2011. Experimental determination of stability relations between monazite, fluorapatite, allanite, and REE-epidote as a function of pressure, temperature, and fluid composition. American Mineralogist 96, 1547–1567.

Budzyń, B., Hetherington, C.J., Williams, M.L., Jercinovic, M.J., Michalik, M., 2010. Fluid-mineral interactions and constraints on monazite alteration during metamorphism. Mineralogical Magazine 74, 4, 659–681

Caruso, L., Simmons, G., 1985. Uranium and microcracks in a 1,000-meter core, Redstone, New Hampshire. Contributions to Mineralogy and Petrology. 90, 1–17.

Chabiron, A., Cuney, M., 2001. Altération de l'allanite dans les granites sous la caldeira de Streltsovka (Transbaïkalie, Russie). Une source possible d'uranium pour les gisement. C. R. Acad. Sci. Paris, Sciences de la Terre et des planètes / Earth and Planetary Sciences 332. 99–105.

508 Corriveau, L., Ootes, L., Mumin, H., Jackson, H., Bennett, V., Cremer, J.F., Rivard, B., McMartin,
509 I., Beaudoin, G., 2007. Alteration vectoring to IOCG(U) deposits in frontier volcano-
510 plutonic terrains, Canada., in: Proceedings of Exploration 07: Fifth Decennial
511 International Conference on Mineral Exploration. B. Milkereit, pp. 1171–1177.
512 Engi, M., 2017. Petrochronology Based on REE-Minerals: Monazite, Allanite, Xenotime, Apatite.
513 Reviews in Mineralogy and Geochemistry 83, 365–418.
514 Ercit, T.S., 2002. The mess that is "Allanite." The Canadian Mineralogist 40, 1411–1419.
515 Ewing, R.C., Chakoumakos, B.C., Lumpkin, G.R., Murakami, T., 1987. The Metamict State.
516 MRS Bulletin.
517 Frugier, P., Gin, S., Minet, Y., Chave, T., Bonin, B., Godon, N., Lartigue, J.-E., Jollivet, P., Ayral,
518 A., De Windt, L., Santarini, G., 2008. SON68 nuclear glass dissolution kinetics: Current
519 state of knowledge and basis of the new GRAAL model. Journal of Nuclear Materials 380,
520 8–21.
521 Gabitov, R., Sadekov, A., Migdisov, A., 2017. REE Incorporation into Calcite Individual Crystals
522 as One Time Spike Addition. Minerals 7, 204.
523 Gammons, C.H., Wood, S.A., Williams-Jones, A.E., 1996. The aqueous geochemistry of the rare
524 earth elements and yttrium: VI. Stability of neodymium chloride complexes from 25 to
525 300°C. Geochimica et Cosmochimica Acta 60, 4615–4630.
526 Gieré, R., Sorensen, S.S., 2004. Allanite and Other REE-Rich Epidote-Group Minerals. Reviews
527 in Mineralogy and Geochemistry 56, 431–493.
528 Gob, S., Wenzel, T., Bau, M., Jacob, D.E., Loges, A., Markl, G., 2011. The redistribution of Rare-
529 Earth Elements in secondary minerals of hydrothermal veins, Schwarzwald, Southwestern
530 Germany. The Canadian Mineralogist 49, 1305–1333.
531 Grand'Homme, A., Janots, E., Seydoux-Guillaume, A.M., Guillaume, D., Magnin, V.,
532 Hövelmann, J., Höschen, C., Boiron, M.C., 2018. Mass transport and fractionation during
533 monazite alteration by anisotropic replacement. Chemical Geology 484, 51–68.
534 Guillong, M., Meier, D.L., Allan, M.M., Heinrich, C.A., Yardley, B.W.D., 2008. SILLS: a
535 Matlab-based program for the reduction of laser ablation ICP-MS data of homogeneous
536 materials and inclusions. Mineralogical Association of Canada Short Course, Vancouver,
537 B.C. Appendix A6, 328–333.

538 Harlov, D.E., Wirth, R., Hetherington, C.J., 2011. Fluid-mediated partial alteration in monazite:
539 the role of coupled dissolution–reprecipitation in element redistribution and mass transfer.
540 Contrib Mineral Petrol 162, 329–348.
541 Heinrich, W., Rehs, G., Franz, G., 1997. Monazite–xenotime miscibility gap thermometry. I. An
542 empirical calibration. Journal of Metamorphic Geology 15, 3–16.
543 Hellmann, R., 1994. The albite-water system: Part I. The kinetics of dissolution as a function of
544 pH at 100, 200, and 300°C. Geochemica et Cosmochemica Acta 58, 595–611.
545 Hellmann, R., Wirth, R., Daval, D., Barnes, J.-P., Penisson, J.-M., Tisserand, D., Epicier, T.,
546 Florin, B., Hervig, R.L., 2012. Unifying natural and laboratory chemical weathering with
547 interfacial dissolution–reprecipitation: A study based on the nanometer-scale chemistry of
548 fluid–silicate interfaces. Chemical Geology 294–295, 203–216.
549 Hentschel, F., Janots, E., Trepmann, C.A., Magnin, V., Lanari, P., 2020. Corona formation around
550 monazite and xenotime during greenschist-facies metamorphism and deformation.
551 European Journal of Mineralogy 32, 521–544.
552 Ichimura, K., Sanematsu, K., Kon, Y., Takagi, T., Murakami, T., 2020. REE redistributions during
553 granite weathering: Implications for Ce anomaly as a proxy for paleoredox states.
554 American Mineralogist 105, 848–859.
555 Jamtveit, B., Putnis, C.V., Malthe-Sørenssen, A., 2009. Reaction induced fracturing during
556 replacement processes. Contributions to Mineralogy and Petrology 157, 127–133.
557 Janots, E., Berger, A., Gnos, E., Whitehouse, M., Lewin, E., Pettke, T., 2012. Constraints on fluid
558 evolution during metamorphism from U–Th–Pb systematics in Alpine hydrothermal
559 monazite. Chemical Geology 326–327, 61–71.
560 Janots, E., Engi, M., Berger, A., Allaz, J., Schwarz, J.-O., Spandler, C., 2008. Prograde
561 metamorphic sequence of REE minerals in pelitic rocks of the Central Alps: implications
562 for allanite–monazite–xenotime phase relations from 250 to 610 °C. Journal of
563 Metamorphic Geology 26, 509–526.
564 Jochum, K.P., Weis, U., Stoll, B., Kuzmin, D., Yang, Q., Raczek, I., Jacob, D.E., Stracke, A.,
565 Birbaum, K., Frick, D.A., Günther, D., Enzweiler, J., 2011. Determination of Reference
566 Values for NIST SRM 610-617 Glasses Following ISO Guidelines. Geostandards and
567 Geoanalytical Research 35, 397–429.

568 Jochum, K.P., Willbold, M., Raczek, I., Stoll, B., Herwig, K., 2005. Chemical Characterisation of
569 the USGS Reference Glasses GSA-1G, GSC-1G, GSD-1G, GSE-1G, BCR-2G, BHVO-
570 2G and BIR-1G Using EPMA, ID-TIMS, ID-ICP-MS and LA-ICP-MS. Geostandards and
571 Geoanalytical Research 29, 285–302.
572 Kalinowski, B.E., Faith-Ell, C., Schweda, P., 1998. Dissolution kinetics and alteration of epidote
573 in acidic solutions at 25°C. Chemical Geology 151, 181–197.
574 Kolonin, G.R., Shironosova, G.P., 2007. REE distribution between fluorite and ore-forming fluid
575 based on results of thermodynamic modeling. Dokl. Earth Sc. 414, 661–665.
576 Krenn, E., Harlov, D.E., Finger, F., Wunder, B., 2012. LREE-redistribution among fluorapatite,
577 monazite, and allanite at high pressures and temperatures. Am. Mineral. 97, 1881–
578 1890. https://doi.org/10.2138/am.2012.4005
579 Lafay, R., Montes-Hernandez, G., Janots, E., Chiriac, R., Findling, N., Toche, F., 2014.
580 Simultaneous precipitation of magnesite and lizardite from hydrothermal alteration of
581 olivine under high-carbonate alkalinity. Chemical Geology 368, 63–75.
582 Lafay, R., Montes-Hernandez, G., Renard, F., Vonlanthen, P., 2018. Intracrystalline Reaction-
583 Induced Cracking in Olivine Evidenced by Hydration and Carbonation Experiments.
584 Minerals 8, 412.
585 Li, Y.H.M., Zhao, W.W., Zhou, M.-F., 2017. Nature of parent rocks, mineralization styles and
586 ore genesis of regolith-hosted REE deposits in South China: An integrated genetic model.
587 Journal of Asian Earth Sciences 148, 65–95.
588 Mezger, K., Essene, E.J., van der Pluijm, B.A., Halliday, A.N., 1993. U-Pb geochronology of the
589 Grenville Orogen of Ontario and New York: constraints on ancient crustal tectonics.
590 Contributions to Mineralogy and Petrology 114, 13–26.
591 Middleton, A.W., Förster, H.-J., Uysal, I.T., Golding, S.D., Rhede, D., 2013. Accessory phases
592 from the Soultz monzogranite, Soultz-sous-Forêts, France: Implications for titanite
593 destabilisation and differential REE, Y and Th mobility in hydrothermal systems.
594 Chemical Geology 335, 105–117.
595 Migdisov, A., Guo, X., Nisbet, H., Xu, H., Williams-Jones, A.E., 2019. Fractionation of REE, U,
596 and Th in natural ore-forming hydrothermal systems: Thermodynamic modeling. The
597 Journal of Chemical Thermodynamics 128, 305–319.

598 Möller, P., Bau, M., Dulski, P., Lüders, V., 1998. REE and yttrium fractionation in fluorite and
599 their bearing on fluorite formation. Proceedings of the Ninth Quadrennial IAGOD
600 Symposium, Schweizerbart, Stuttgart 575–592.
601 Montes-Hernandez, G., Chiriac, R., Toche, F., Renard, F., 2012. Gas–solid carbonation of
602 Ca(OH)2 and CaO particles under non-isothermal and isothermal conditions by using a
603 thermogravimetric analyzer: Implications for CO2 capture. International Journal of
604 Greenhouse Gas Control 11, 172–180.
605 Nisbet, H., Migdisov, A., Xu, H., Guo, X., van Hinsberg, V., Williams-Jones, A.E., Boukhalfa,
606 H., Roback, R., 2018. An experimental study of the solubility and speciation of thorium
607 in chloride-bearing aqueous solutions at temperatures up to 250 °C. Geochimica et
608 Cosmochimica Acta 239, 363–373.
609 Nisbet, H., Migdisov, A.A., Williams-Jones, A.E., Xu, H., van Hinsberg, V.J., Roback, R., 2019.
610 Challenging the thorium-immobility paradigm. Scientific Reports 9, 17035.
611 Ondrejka, M., Bačík, P., Sobocký, T., Uher, P., Škoda, R., Mikuš, T., Luptáková, J., Konečný, P.,
612 2018. Minerals of the rhabdophane group and the alunite supergroup in microgranite:
613 products of low-temperature alteration in a highly acidic environment from the Velence
614 Hills, Hungary. Mineral. Mag. 82, 1277–1300. https://doi.org/10.1180/mgm.2018.137
615
616 Pal, D.C., Chaudhuri, T., McFarlane, C., Mukherjee, A., Sarangi, A.K., 2011. Mineral Chemistry
617 and In Situ Dating of Allanite, and Geochemistry of Its Host Rocks in the Bagjata Uranium
618 Mine, Singhbhum Shear Zone, India—Implications for the Chemical Evolution of REE
619 Mineralization and Mobilization. Economic Geology 106, 1155–1171.
620 Pekov, I.V., Krivovichev, S.V., Zolotarev, A.A., Yakovenchuk, V.N., Armbruster, T.,
621 Pakhomovsky, Y.A., 2009. Crystal chemistry and nomenclature of the lovozerite group.
622 European Journal of Mineralogy 21, 1061–1071.
623 Perry, E.P., Gysi, A.P., 2018. Rare Earth Elements in Mineral Deposits: Speciation in
624 Hydrothermal Fluids and Partitioning in Calcite. Geofluids 2018, 1–19.
625 Pettke, T., Oberli, F., Audétat, A., Wiechert, U., Harris, C.R., Heinrich, C.A., 2011. Quantification
626 of transient signals in multiple collector inductively coupled plasma mass spectrometry:
627 accurate lead isotope ratio determination by laser ablation of individual fluid inclusions.
628 Journal of Analytical Atomic Spectrometry 26, 475–492.

629 Poitrasson, F., 2002. In situ investigations of allanite hydrothermal alteration: examples from calc-
630 alkaline and anorogenic granites of Corsica (southeast France). Contributions to
631 Mineralogy and Petrology 142, 485–500.
632 Poitrasson, F., Chenery, S., Shepherd, T.J., 2000. Electron microprobe and LA-ICP-MS study of
633 monazite hydrothermal alteration: implications for the U-Th-Pb geochronology and nuclear
634 ceramics. Geochim. Cosmochim. Acta, 64, 3283-3297.
635 Price, J.R., Velbel, M.A., Patino, L.C., 2005. Allanite and epidote weathering at the Coweeta
636 Hydrologic Laboratory, western North Carolina, U.S.A. American Mineralogist 90, 101–
637 114.
638 Putnis, A., 2009. Mineral Replacement Reactions. Reviews in Mineralogy and Geochemistry 70,
639 87–124.
640 Putnis, A., 2002. Mineral replacement reactions: from macroscopic observations to microscopic
641 mechanisms. Mineralogical Magazine 66, 689–708.
642 Putnis, A., Putnis, C.V., 2007. The mechanism of reequilibration of solids in the presence of a
643 fluid phase. Journal of Solid State Chemistry 180, 1783–1786.
644 Rai, D., Felmy, A.R., Moore, D.A., Mason, M.J., 1994. The Solubility of Th(IV) and U(IV)
645 Hydrous Oxides in Concentrated Nahco $_3$ and Na $_2$ Co $_3$ Solutions. MRS Proceedings 353,
646 1143.
647 Rimstidt, J.D., Balog, A., Webb, J., 1998. Distribution of trace elements between carbonate
648 minerals and aqueous solutions. Geochimica et Cosmochimica Acta 62, 1851–1863.
649 Rose, N.M., 1991. Dissolution rates of prehnite, epidote, and albite. Geochimica et Cosmochimica
650 Acta 55, 3273–3286.
651 Ruiz-Agudo, E., King, H.E., Patiño-López, L.D., Putnis, C.V., Geisler, T., Rodriguez-Navarro,
652 C., Putnis, A., 2016. Control of silicate weathering by interface-coupled dissolution-
653 precipitation processes at the mineral-solution interface. Geology 44, 567–570.
654 Ruiz-Agudo, E., Putnis, C.V., Putnis, A., 2014. Coupled dissolution and precipitation at mineral–
655 fluid interfaces. Chemical Geology 383, 132–146.
656 Ruiz-Agudo, E., Putnis, C.V., Rodriguez-Navarro, C., Putnis, A., 2012. Mechanism of leached
657 layer formation during chemical weathering of silicate minerals. Geology 40, 947–950.

Sandino, A., Bruno, J., 1998. The solubility of (UO2)3(PO4)2.4H20(s) and the formation of U(VI) phosphate complexes: Their influence in uranium speciation in natural waters. Geochemica et Cosmochemica Acta 56, 11.

Schönenberger, J., Köhler, J., Markl, G., 2008. REE systematics of fluorides, calcite and siderite in peralkaline plutonic rocks from the Gardar Province, South Greenland. Chemical Geology 247, 16–35.

Schwinn, G., Markl, G., 2005. REE systematics in hydrothermal fluorite. Chemical Geology 216, 225–248.

Seward, T.M., Williams-Jones, A.E., Migdisov, A.A., 2014. The Chemistry of Metal Transport and Deposition by Ore-Forming Hydrothermal Fluids, in: Treatise on Geochemistry. Elsevier, pp. 29–57.

Smith, M.P., Henderson, P., Jeffries, T., 2002. The formation and alteration of allanite in skarn from the Beinn an Dubhaich granite aureole, Skye. European Journal of Mineralogy 14, 471–486.

Stipp, S.L.S., Christensen, J.T., Lakshtanov, L.Z., Baker, J.A., Waight, T.E., 2006. Rare Earth element (REE) incorporation in natural calcite: Upper limits for actinide uptake in a secondary phase. Radiochimica Acta 94.

Toyama, K., Terakado, Y., 2014. Experimental study of rare earth element partitioning between calcite and sodium chloride solution at room temperature and pressure. Geochemical Journal 48, 463–477.

van Hinsberg, V.J., Migdisov, A.A., Williams-Jones, A.E., 2010. Reading the mineral record of fluid composition from element partitioning. Geology 38, 847–850.

Xu, C., Taylor, R.N., Li, W., Kynicky, J., Chakhmouradian, A.R., Song, W., 2012. Comparison of fluorite geochemistry from REE deposits in the Panxi region and Bayan Obo, China. Journal of Asian Earth Sciences 57, 76–89.

Zaitsev, A.N., Demény, A., Sindern, S., Wall, F., 2002. Burbankite group minerals and their alteration in rare earth carbonatites—source of elements and fluids (evidence from C–O and Sr–Nd isotopic data). Lithos 62, 15–33.

Figure Captions

Figure 1. Evolution of the proportion of the starting material and run products, utilizing Rietveld refinement (in %) for initial acidic (**a**) and high pH alkaline (**b**) F-doped systems. The group of REE-carb represents bastnäsite + synchysite in acidic system, and parisite + bastnäsite + synchysite + the burbankite-groupe mineral in the high pH alkaline system. These REE-carbonate minerals were identified by XRD analyses. Full lines represent the maximum allanite replacement in a state close to equilibrium. Numerical values are presented in Table 1. Aln = allanite; Ana = analcime; Cal = calcite; Fl = fluorite; Hem = hematite; Nrd = nordstrandite; Sme = smectite.

Figure 2. Scanning electron microscopy images using backscattered electron (BSE) imaging of allanite and secondary products from acidic (a, b, and c) and high pH alkaline (d, e, and f) F-doped runs for different times. **a.** Relatively unaltered allanite with fluorite and analcime growing along the allanite grain rims. **b.** Relatively unaltered allanite (top left) with internal fractures filled by REE-phases along with more reacted allanite (bottom right) with sawtooth-shaped grain rims after 120 days. **c.** Magnification of b showing reaction interface with allanite composed of granular nanometric REE-fluorocarbonates replacing allanite. **d**. Allanite grain displaying edge pitting with a porosity that progresses anisotropically to the grain center. Edges are rimmed by a saponite whiskers, which probably formed during quenching. **e**. Detail of an allanite edge showing a sharp eroded surface rimmed by REE-fluorocarbonates with a granular, prismatic, and needle-like shape, along with hematite and saponite. Porous cavities are filled with REE fluorocarbonates **f.** Cluster of Burbankite-group minerals with a large crystal of calcite growing in the interstitial space between the minerals. Aln = allanite; Ana = analcime; Bgm = burbankite-group mineral; Cal = calcite; Fl = fluorite; Hem = hematite; REE-FCb = REE-fluorocarbonates (bastnäsite, parisite, synchysite); Sap = saponite; Sme = smectite.

Figure 3. Comparison of mineral modal compositions after 120 days for the F-doped high pH alkaline systems and the F-, P-, S-, and Cl-doped systems (respectively shown in columns), which

were identified by X-ray diffraction (XRD) and Rietveld refinement (in %). Aln = allanite; Ana = analcime; Anh = anhydrite; Cal = calcite; Fl = fluorite; Hal = halite; Hap = hydroxylapatite; Hem = hematite; Mnz = monazite; Nrd = nordstrandite; Sme = smectite.

Figure 4. Secondary electron (SE) and backscattered electron (BSE) images of allanite alteration in an acidic P-doped system. **a**. Typical allanite grain with eroded grain boundaries and with large crystals of analcime partially embedding the other secondary minerals. **b**. Continuous reaction front composed of monazite replacing allanite and a thin (< 200 nm) rim of hematite outlining the original shape of the allanite. Outwards from the reaction front is rimmed by euhedral hydroxyapatite (Hap) that precipitated in the interstitial space between filaments of saponite (Sap). **c**. Detail from **b** showing that the abundance of the nano-size monazite increases in the vicinity of the eroded allanite. Aln = allanite; Ana = analcime; Cal = calcite; Hap = hydroxylapatite; Hem = hematite Mnz = monazite; Sap = saponite.

Figure 5. Major elements, REE, and actinide concentrations (log) in experimental fluids for the time series F-doped experiments in the acidic system (**a**), high pH alkaline system (**b**), and in the 120 day experiments for the P-, S-, and Cl-doped systems (**c**).

Figure 6. Chondrite-normalized REE spectra of fluids after 120 days from the slightly acidic, F-doped, P- doped, S- doped, Cl-doped, and time series, high pH alkaline, F-doped experiments. The HREE with odd numbers are below the detection limits or have been removed from the diagram because of artificial anomalies due to being close to the detection limits (Table 1). The lanthanide tetrad effect is discernible within the LREE for the slightly acid experiments (dashed lines).

Table 1. Experimental conditions and solid products

Set	Exp.	Carbonate source	Initial pH	Ligands (120 mM)	Duration (days)	Aln (%)	Secondary solid products
B1	B1015	Carbonic ice[1]	4	NaF	15	93	Bsn (1.2%); Syn (1.5%); Flr (2.0%); Hem (2.1%);
	B1030	Carbonic ice[1]	4	NaF	30	92	Bsn (2.2%); Syn (1.0%); Flr (2.5%); Hem (2.0%);
	B1060	Carbonic ice[1]	4	NaF	60	95	Bsn (3.2%); Flr (3.6%); Hem (2.4%); Ana (4.9%);
	B1120	Carbonic ice[1]	4	NaF	120	76	Bsn (5.1%); Syn (< 1%); Flr (4.3%); Hem (2.2%); Ana (12%);
	B1180	Carbonic ice[1]	4	NaF	180	77	Bsn (5.6%); Flr (5.8%); Hem (4.7%); Ana (7.3%);
B2	B2015	$NaHCO_3^-$ 1M 1.5mL	8.7	NaF	15	36	Bsn (2.0%); Syn (1.0%); Pst (6.6%); BGM (8.9%); Cal (4.5%); Hem (8.9%); Ana (22%); Sme (6.7%); Nsd (3.1%)
	B2030	$NaHCO_3^-$ 1M 1.5mL	8.7	NaF	30	29	Bsn (3.1%); Syn (1.0%); Pst (8.9%); BGM (5.7%); Cal (4.5%); Hem (8.4%); Ana (26%); Sme (7.7%); Nsd (4.1%)
	B2060	$NaHCO_3^-$ 1M 1.5mL	8.7	NaF	60	31	Bsn (3.1%); Syn (1.7%); Pst (8.9%); BGM (9.4%); Cal (8.4%); Hem (9.1%); Ana (24%); Sme (7.6%); Nsd (1.8%)
	B2120	$NaHCO_3^-$ 1M 1.5mL	8.7	NaF	120	23	Bsn (5.2%); Syn (< 1%); Pst (3.3%); BGM (5.9%); Cal (9.5%); Hem (9.9%); Ana (31%); Sme (7.2%); Nsd (3.8%)
B3	B3P120	Carbonic ice[1]	4	$Na_3PO_4.12H_2O$	120	27	Mnz (15%); Hap (13%); Hem (6.8%); Ana (31%); Sme (6.3%)
	B3S120	Carbonic ice[1]	4	Na_2SO_4	120	97	Anh (1.6%); Ana (1.6%)
	B3Cl120	Carbonic ice[1]	4	NaCl	120	98	Hl (2.0%)

Carbonic ice is certified 100% pure CO_2 – around 30 mg (after the epoxy reactor closure). Estimated standard deviation is < 2% for values > 10% and does not exceed 10% for lower quantification. Aln = allanite; Ana = analcime; Anh = anhydrite; BGM = burbankite-group mineral; Bsn = bastnäsite; Cal = calcite; Chl = chlorite; Flr = fluorite; Hap = hydroxyapatite; Hem = hematite; Hl = halite; Mnz = monazite; Nsd = nordstrandite; Pst = parisite; Sme = smectite; Syn = synchysite. For a better reading comprehension with Aln (allanite), Ana designate analcime instead of the common abbreviation Anl. Abbreviation from Warr L.N. (2021) IMA–CNMNC approved mineral symbols. Mineralogical Magazine 85, 291–320.

Table 2. Microprobe selected analyses of major run products (wt%).

	Analcime		**Calcite**		**BGM**		**Fluorite**		**Anhydrite**
System	HCO_3^- + F^-	CO_2 + PO_4^{2-}	HCO_3^- + F^-		HCO_3^- + F^-		CO_2 + F^-		CO_2 + SO_4^{2-}
Days	120	120	120	120	120	120	120	180	120
SiO_2	49.1	49.0							
Al_2O_3	24.5	24.1					0.22	0.32	
FeO	0.09	0.13	0.23	0.32	0.54		0.09	0.21	0.10
CaO			51.2	53.0	21.08	6.07	66.35	67.05	41.75
Na_2O	15.8	15.2	0.62	0.39	0.37	1.66	0.5	0.51	0.05
P_2O_5		0.15	0.12				0.14	0.18	
SO_3									47.47
F			0.30		0.18	0.57	48.02	47.75	
La_2O_3			1.90	0.90	14.69	15.17	0.68	0.35	0.17
Ce_2O_3			4.13	2.30	23.51	30.52	1.20	0.69	0.51
Pr_2O_3			0.46	0.24	1.68	2.57	0.19	-	0.14
Nd_2O_3			1.16	0.60	3.56	6.35	0.23	0.12	0.16
Sm_2O_3									
Gd_2O_3		0.13	0.21						
Dy_2O_3					0.23				
Y_2O_3			0.12	0.11			0.12		
SrO			0.25	0.26	1.02	0.68	1.62	1.59	0.61
ThO_2			0.09	0.15	0.84	0.90	0.27		
PbO						0.13			
Total[1]	89.50	88.66	60.63	58.27	67.63	64.37	99.41	98.68	90.94
∑(REE)[2]		0.13	7.99	4.16	43.68	54.60	2.42	1.17	0.97
La/Y	n.d.	n.d.	17.4	8.79	n.d.	n.d.	6.02	n.d.	n.d.
Ce/Ce*[3]	n.d.	n.d.	1.07	1.19	1.14	1.18	0.8	2.84	0.82

Notes: Values in italic (%) column are mean relative errors, and 2σ is the standard deviation; n.d. not determined; [1] Total is corrected of -O=F_2 values; [2] ∑REE refers to the sum of $(REE+Y)_2O_3$; [3] Ce/Ce* $CeN/(LaN*PrN)^{1/2}$. Empty cells are concentrations below detection. n.d. not determined

Table 3. Composition of fluids after allanite batch experiments

		Experimental set											
	System	**CO_2 + F^-**					**$NaHCO_3$ + F^-**				**CO_2 + PO_4^{2-}**	**CO_2 + SO_4^{2-}**	**CO_2 + Cl^-**
	Experiment	B1015	B1030	B1060	B1120	B1180	B2015	B2030	B2060	B2120	B3P120	B3S120	B3Cl120
	Days	15	30	60	120	180	15	30	60	120	120	120	120
mol /kg x10^{-4}	[1] Si	38.0	15.8	13.1	16.8	16.0	19.4	22.3	25.4	43.0	62.1	14.9	27.4
	Al	1.20	1.35	0.51	5.88	5.76	2.40	2.06	1.50	0.50	2.48	0.35	0.11
	Fe						0.21	0.20	0.16	0.12	0.045		
	Ca				0.11	0.069	0.14	0.14	0.16	0.17	0.082		0.077
	Respective ligands	950	976	869	668	598	1781	1661	1412	1211		1477	2877
	HCO_3^-						10980	10791	7132	6604	2489		
mol /kg x10^{-8}	Y				4.34	0.20	140	175	227	297	4.85	0.26	1.27
	La		0.25	0.40	4.49	1.51	30.3	24.8	41.6	52.9	15	4.90	2.88
	Ce	0.07	0.25	0.35	6.48	5.28	81.4	73.5	94.2	75.1	8.04	1.92	0.93
	Pr			0.033	0.48	0.23	9.50	11.3	12.5	14.8	1.14	0.27	0.25
	Nd				1.97	0.52	37.2	45.6	49.1	55.6	5.23	0.94	4.26
	Sm				0.24	0.037	9.26	11.4	11.8	12.7	0.44	0.04	0.19
	Eu				0.21		1.69	2.10	2.22	2.59	0.36	0.02	0.20
	Gd				0.45	0.077	9.80	12.1	13.8	15.3	0.76	0.06	0.25
	Tb				0.0031		1.70	2.15	2.54	2.85	0.013	0.0022	0.0035
	Dy				1.13		10.9	14.0	16.7	19.6	1.21	0.045	0.38
	Ho						2.45	3.15	3.84	4.55			
	Er				2.25		8.89	11.7	13.5	16.6	2.15	0.073	0.67
	Tm						1.64	2.12	2.33	2.59			
	Yb				3.26		13.6	17.6	17.6	20.2	2.67	0.094	1.05
	Lu						2.69	3.47	3.31	3.59			
	Th		0.0077	0.033	0.24	0.24	349	216	304	193	0.30	0.025	
	U	16.0	18.1	4.89	8.76	12.4	2795	2972	2570	3120	6.54		

Respective ligands refer to the anion initially used for the experiments (measured as F^-, PO_4^{3-}, SO_4^{2-}, Cl^-). Maximum analytical error is < 4% for Si, La, Ce, Pr, Ho, Tm; < 8 % for Al, Fe, Eu, Lu, Y, Th; 9% for U; < 15% for Nd, Sm, Yb, < 19% for Gd, Eu; 34% for Ca. Empty cells are concentrations below detection.

figure 1

Click here to access/download;figure;Fig.1_XRD.jpg

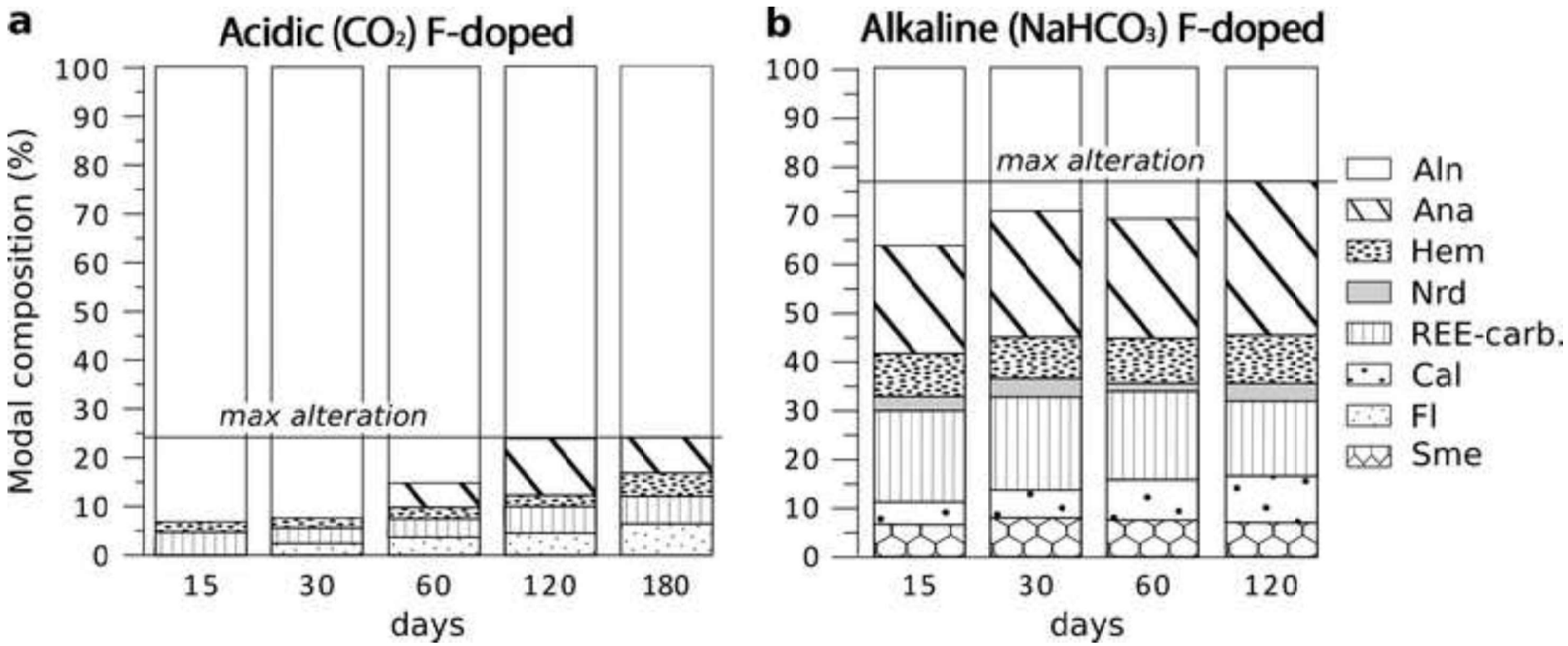

figure 2

Click here to access/download;figure;Fig.2_review202302.jpg

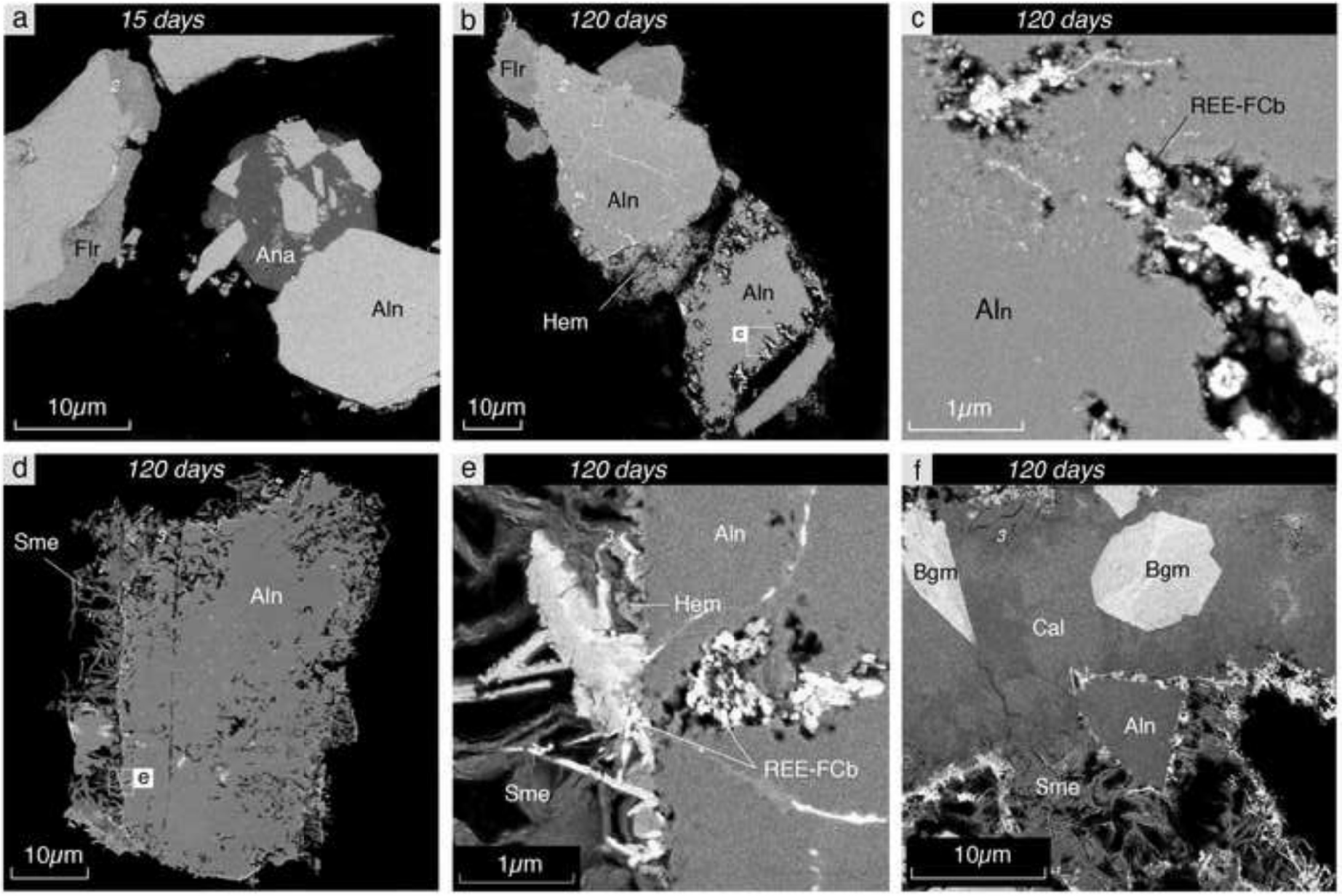

figure 3

Click here to access/download;figure;Fig.3_XRD.jpg

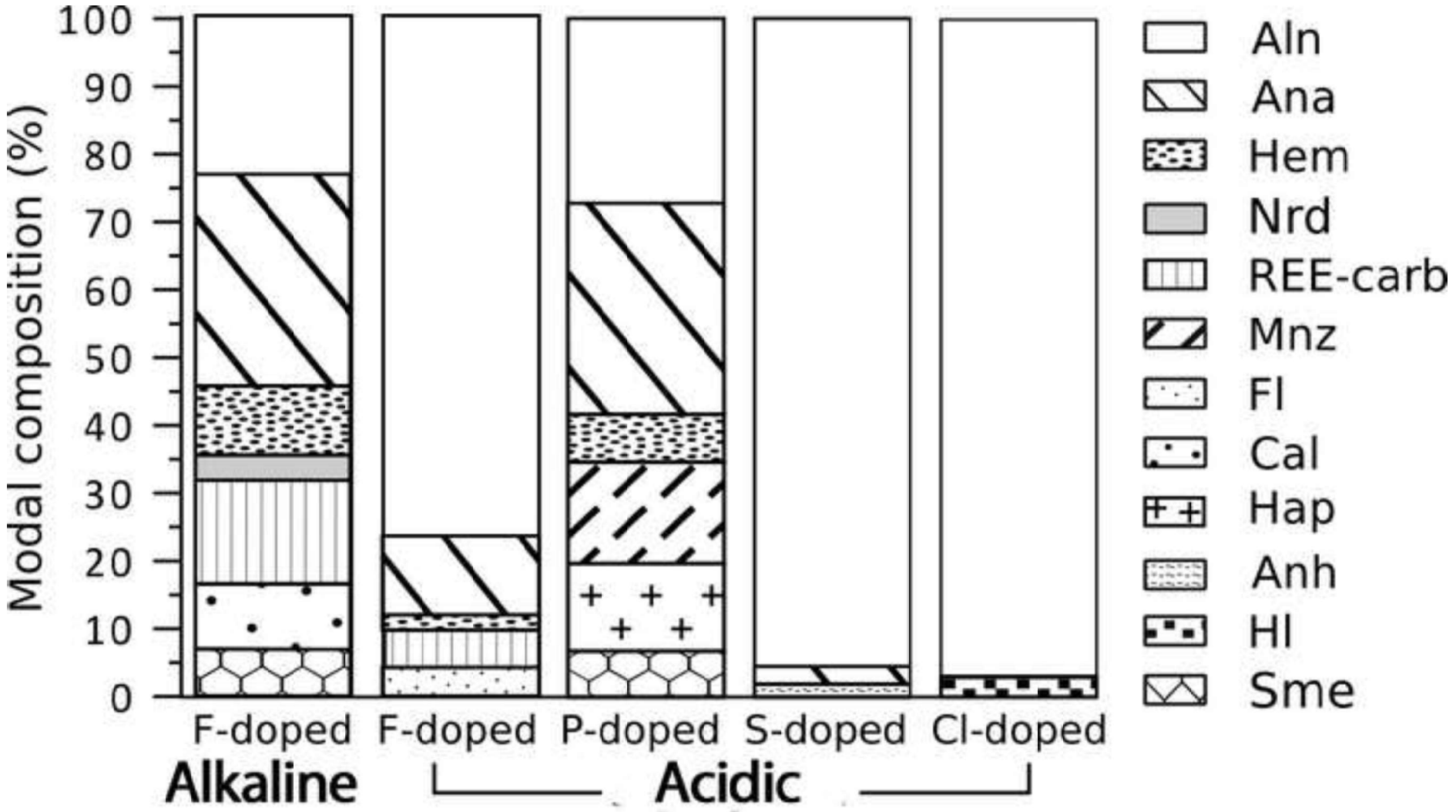

figure 4

Click here to access/download;figure;Fig_4.png

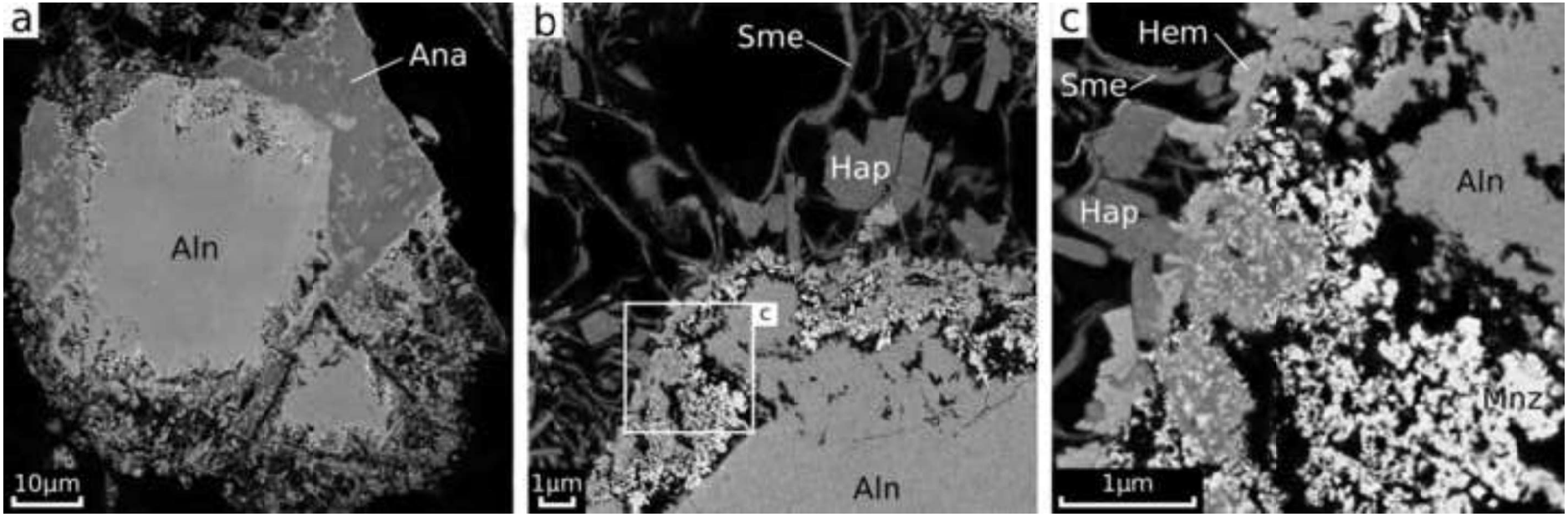

figure 5

Click here to access/download;figure;Fig 5.jpg

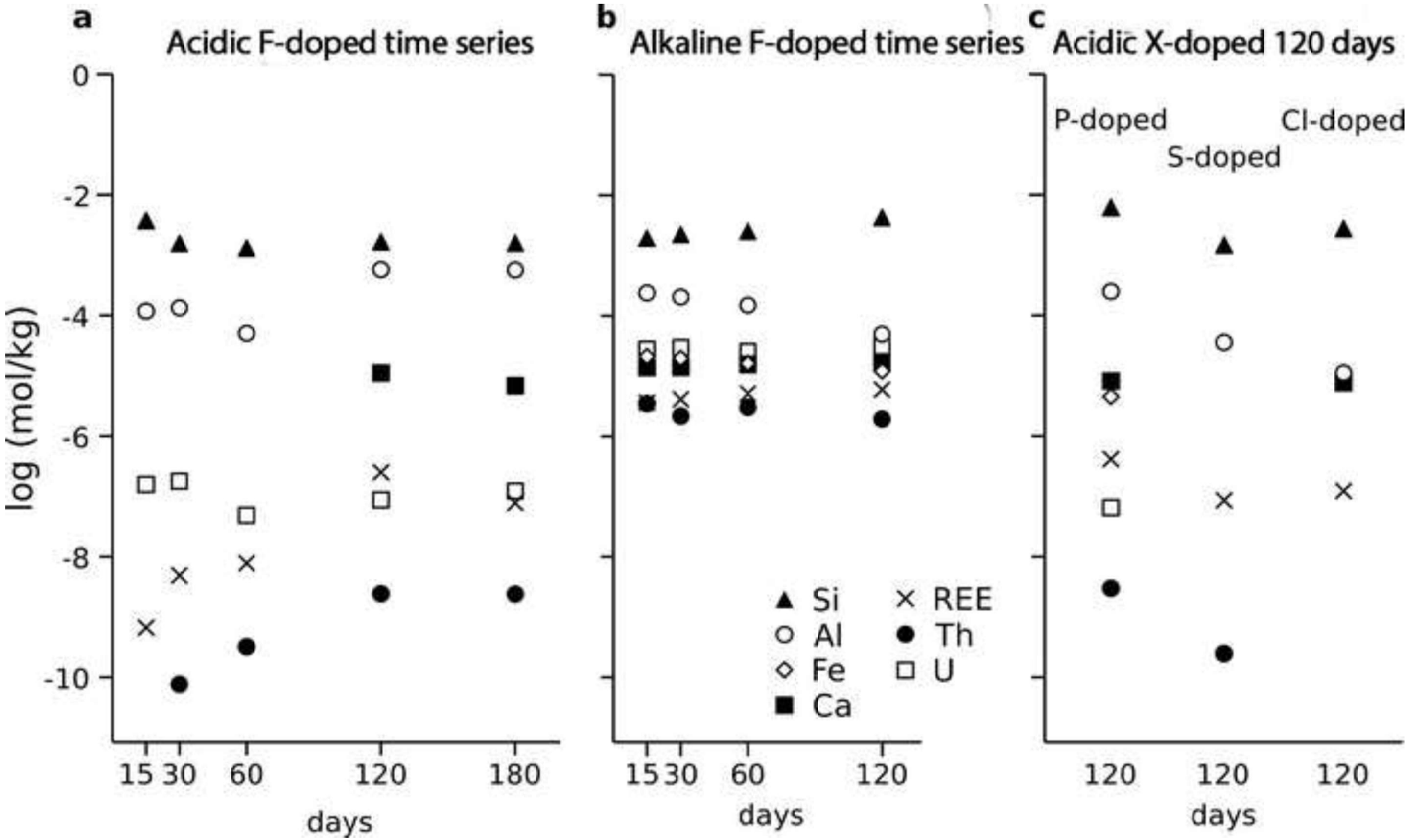

figure 6

Click here to access/download;figure;Fig 6.jpg

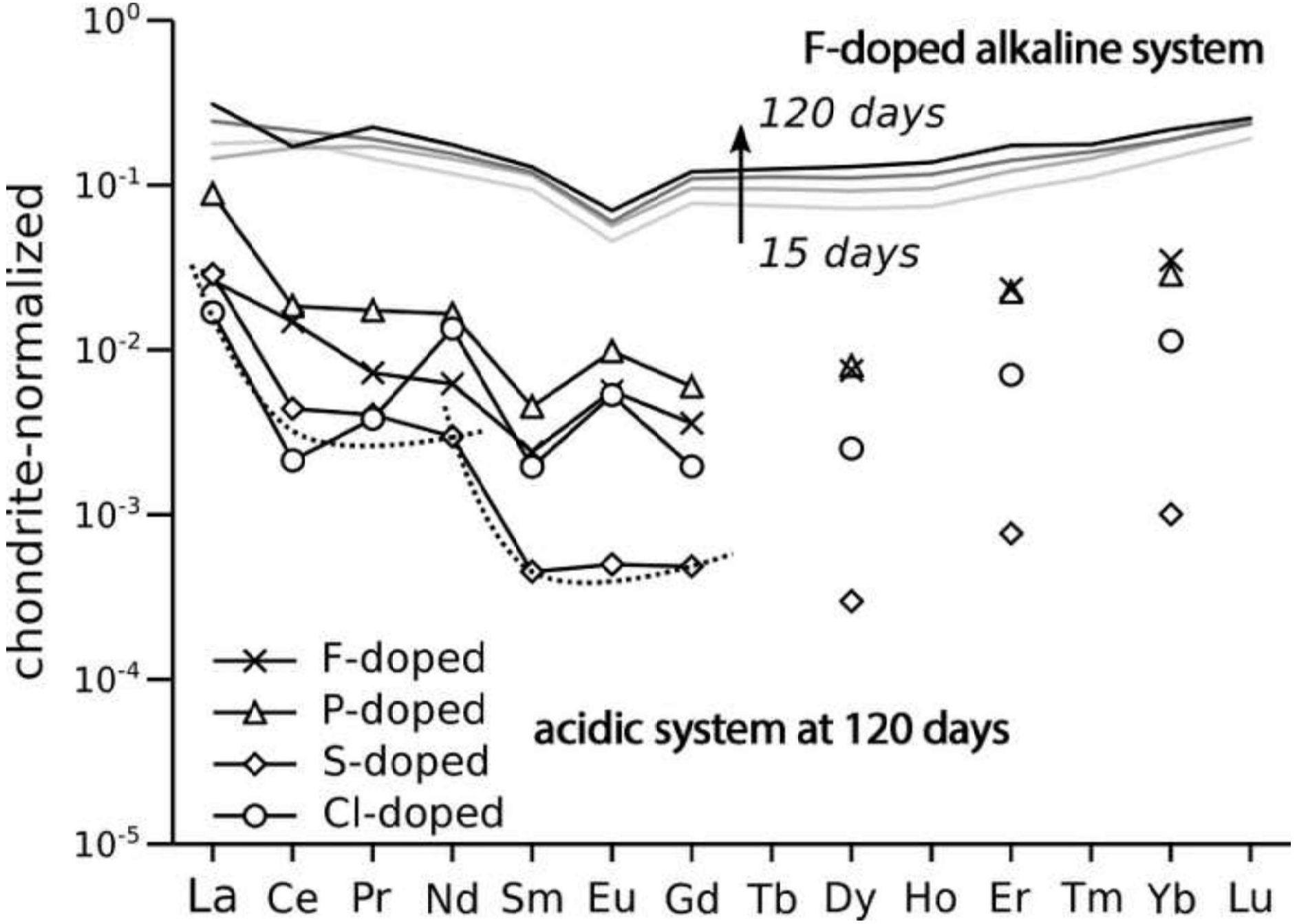

supplementary material

Click here to access/download

supplementary material

Copie de supp-data-S1-S2-S3_AD.xlsx

supplementary material